



Kr II and Xe II axial velocity distribution functions in a cross-field ion source

A. Lejeune, G. Bourgeois, and S. Mazouffre

Citation: *Phys. Plasmas* **19**, 073501 (2012); doi: 10.1063/1.4731688

View online: <http://dx.doi.org/10.1063/1.4731688>

View Table of Contents: <http://pop.aip.org/resource/1/PHPAEN/v19/i7>

Published by the [American Institute of Physics](#).

Related Articles

On the anomalous diffusion in nonisothermal plasma
Phys. Plasmas **19**, 072104 (2012)

Linear and nonlinear studies of velocity shear driven three dimensional electron-magnetohydrodynamics instability
Phys. Plasmas **19**, 072103 (2012)

Non-inductive current start-up assisted by energetic electrons in Q-shu University experiment with steady-state spherical tokamak
Phys. Plasmas **19**, 062508 (2012)

Ion stochastic heating by obliquely propagating magnetosonic waves
Phys. Plasmas **19**, 062111 (2012)

Dynamic characteristics of gas-water interfacial plasma under water
Phys. Plasmas **19**, 063507 (2012)

Additional information on *Phys. Plasmas*

Journal Homepage: <http://pop.aip.org/>

Journal Information: http://pop.aip.org/about/about_the_journal

Top downloads: http://pop.aip.org/features/most_downloaded

Information for Authors: <http://pop.aip.org/authors>

ADVERTISEMENT

The advertisement banner for AIP Advances. It features the AIP Advances logo at the top, which consists of the text 'AIP Advances' in a green font with a series of orange dots above it. Below the logo, the text 'Special Topic Section: PHYSICS OF CANCER' is displayed in white on a dark green background. At the bottom, the text 'Why cancer? Why physics?' is written in white, and a blue button with the text 'View Articles Now' is located on the right side.

AIP Advances

Special Topic Section:
PHYSICS OF CANCER

Why cancer? Why physics? [View Articles Now](#)

Kr II and Xe II axial velocity distribution functions in a cross-field ion source

A. Lejeune, G. Bourgeois, and S. Mazouffre

ICARE, CNRS, 1C Avenue de la Recherche Scientifique, 45071 Orlans Cedex 2, France

(Received 12 March 2012; accepted 10 May 2012; published online 3 July 2012)

Laser induced fluorescence measurements were carried out in a cross-field ion source to examine the behaviour of the axial ion velocity distribution functions (VDFs) in the expanding plasma. In the present paper, we focus on the axial VDFs of Kr II and Xe II ions. We examine the contourplots in a 1D-phase space (x, v_x) representation in front of the exhaust channel and along the centerline of the ion source. The main ion beam, whose momentum corresponds to the ions that are accelerated through the whole potential drop, is observed. A secondary structure reveals the ions coming from the opposite side of the channel. We show that the formation of the neutralized ion flow is governed by the annular geometry. The assumption of a collisionless shock or a double layer due to supersonic beam interaction is not necessary. A non-negligible fraction of slow ions originates in local ionization or charge-exchange collision events between ions of the expanding plasma and atoms of the background residual gas. Slow ions that are produced near the centerline in the vicinity of the exit plane are accelerated toward the source body with a negative velocity leading to a high sputtering of front face. On the contrary, the ions that are produced in the vicinity of the channel exit plane are partially accelerated by the extended electric field. © 2012 American Institute of Physics. [<http://dx.doi.org/10.1063/1.4731688>]

I. INTRODUCTION

Ion sources are nowadays studied to ensure the development of ion and atom beam technologies.¹ A major industrial application occurs in the microelectronics industry, where such sources are used for semiconductor ion implantation or thin coating deposition. Ion sources have wide-ranging applications in medicine, laser-driven particle accelerators,² magnetic fusion with neutral beam injectors,³ and space propulsion with gridded ion engines and Hall effect thrusters (HETs).⁴ In this contribution, the investigated ion source is a laboratory model 200 W Hall effect thruster. HETs are propulsion devices for maneuvers such as geo-stationary satellite orbit correction and station keeping. They are well-suited for long duration and large velocity increment missions.⁵ A HET is a plasma discharge that is generated in a dielectric annular chamber where a crossed electric and magnetic field configuration is established. The electrons are magnetized since their Larmor radius is much smaller than the size of the chamber. On the contrary, the ions are unmagnetized and accelerated by the electrostatic force. They are thus expelled outside the chamber, generating the thrust.^{4,6,7} The propellant usually used for HETs is xenon (Xe) due to its high atomic mass (131.3 amu), and its low first ionization energy (12.1 eV). For the past few years, this noble gas has been extensively used in the lighting industry as well as in the medical area. Therefore, its cost has significantly increased, with large price fluctuations on the market, leading the space industry to search for an alternative propellant.⁸ The noble gas with the next highest atomic mass following xenon in the Mendeleiev table is radon (Rn), which is radioactive, and we naturally therefore focus on krypton (Kr). This noble gas has a lower atomic mass (83.8 amu) and a higher first ionization energy (14 eV) in comparison with Xe, but a lower cost. Performance studies have been previously carried out¹⁰ in Xe with the HET

presented in this paper. Laser induced fluorescence (LIF) spectroscopy has been also applied in Kr (Ref. 11) to explore the maximum velocity accelerating profile related to the electric field. The performances in Kr are expected to be lower than in Xe since the ionization energy is higher in Kr and the smaller mass for the Kr II ions reduces the transit time in the channel. The motivation of this work is to explore in space by LIF spectroscopy the axial ion velocity distribution functions (IVDFs) within the plasma plume in Kr and Xe. IVDFs give information about divergence, charge-exchange collisions, ionization, and accelerating patterns, which are crucial points for the thrust performances.

II. EXPERIMENTAL SET-UP AND MEASURED SPECTRA

A. The cross-field ion source

The ion source is a 200 W-class permanent-magnet Hall effect thruster named PPI for “Petit Propulseur Innovant.”¹² The discharge chamber is a dielectric annular channel characterized by its length L , its width h , and its mean diameter d , as depicted in Figure 1. Channel walls are made of alumina (Al_2O_3). The electrons are emitted from an external hollow cathode whose potential is floating. The anode is a metal ring placed at the back of the channel and positively biased to collect the electrons. The total potential difference is called the discharge voltage (V_d). A magnetic field \mathbf{B} is applied through a soft iron magnetic circuit. The magnetic flux is generated by samarium cobalt (SmCo) permanent magnets. The ion source is placed inside a vacuum chamber whose operating pressure is about 10^{-5} mbar (Xe). When the discharge is established, the plasma closes the electric circuit, and the electrons flow from the cathode to the anode. The discharge current (I_d) depends on the operating point

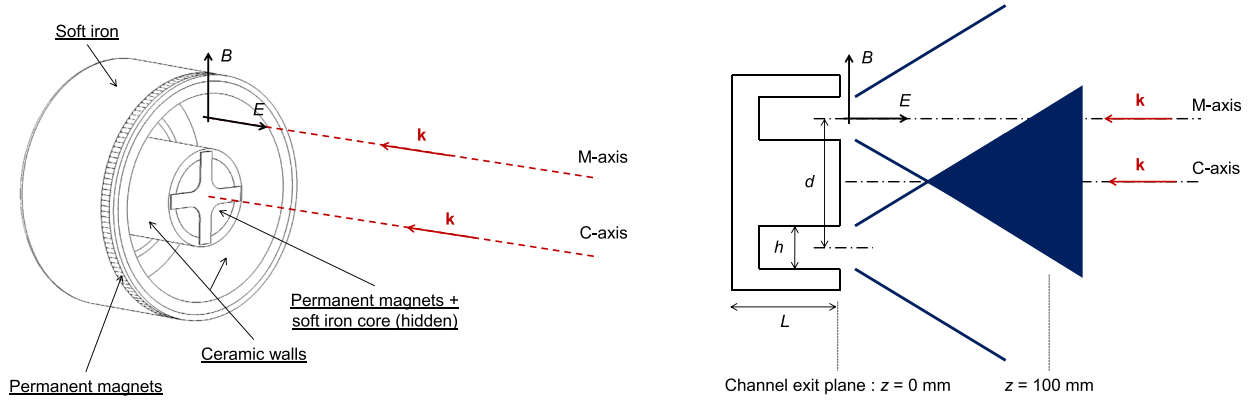


FIG. 1. Global view of the cross-field ion source (left) and scheme of the plasma plume (right); \mathbf{k} is the laser wave vector. Figures are not to scale. LIF measurements were taken at axial positions several times the source diameter.

(V_d, \dot{m}), where \dot{m} is the anode mass flow rate. The ion beam is accelerated away from the anode and forms the plasma plume. In the following experiments, the source was operated in krypton and xenon at a power of 200 W, with $V_d = 200$ V and $I_d = 1$ A. The anode mass flow rate was 11.6 sccm in Xe (1.14 mg/s) and 16.8 sccm in Kr (1.04 mg/s). The cathode was fed with the same gas as that injected in the ion source. The cathode mass flow rate was 2 sccm in Xe (0.2 mg/s) and 4 sccm in Kr (0.2 mg/s).

B. The LIF spectroscopy diagnostic

The LIF spectroscopy technique has been extensively used to measure the ion velocity within the plasma plume of Hall thrusters.^{13,14,16} The laser bench used in this study has been described in previous works.¹¹ The excitation is achieved using a near-infrared continuous tunable laser diode that delivers up to 750 mW light power in the 810–840 nm spectral domain. A fraction of the laser beam is observed on a Fabry-Pérot interferometer to ensure a single-mode regime. The intensity and the wavelength of the laser light are measured, respectively, with a photodiode and a high precision wavemeter (80 MHz). The uncertainty in velocity is about 60 m/s. For phase-sensitive detection, a mechanical chopper is placed along the optical path to modulate the laser beam at 1.5 kHz. The laser beam is transported from the optical bench to the vacuum chamber through a glass window, up to the exit plane of the ion source. In the present work, the laser beam is directed either along the axis (mean diameter; M-axis) or along the ion source centerline (C-axis) as depicted in Figure 1. Note that $\mathbf{k} \cdot \mathbf{v} < 0$ here, with $k = 2\pi/\lambda$. The IVDFs are acquired by scanning the laser wavelength λ over the line shape. The axial velocity v is given by the Doppler shift: $v = c(\lambda - \lambda_0)/\lambda_0$, where λ_0 is the transition wavelength in a vacuum for an ion at rest.¹⁷ The fluorescence light is collected perpendicular to the laser beam axis using a lens that focuses the diagnosed volume image on an optic fiber. The spatial resolution is given by the diameter of the optic fiber (200 μm). The optic fiber brings the fluorescence light back onto the optical bench. The signal goes first through a monochromator that isolates the fluorescence line from the background continuum. It is then collected on a photomultiplier tube. The signal-to-noise ratio is improved using a lock-in amplifier.

C. LIF spectra

The plasma source is mounted onto a translation stage that allows the measurement of the axial velocities from the channel exit plane to 100 mm downstream. In the present paper, we compare the IVDFs measured by LIF spectroscopy on Kr II and Xe II. Table I gives the energy scheme in xenon²¹ to induce the fluorescence at 541.915 nm. This scheme was extensively used and described in previous works.¹⁴ It provides a good signal due to a large population in the $5d^4F_{7/2}$ metastable state of Xe II and a favorable branching ratio. We use a very similar scheme²⁰ for the $4d^4F_{7/2}$ metastable state of Kr II (see Table I) for which the fluorescence is given at 461.917 nm. Note that recently Hargus and co-workers performed LIF measurements on Kr II using the $5d^4D_{7/2} - 5p^4P_{7/2}^0$ transition at 728.98 nm for which the hyperfine structure is known.¹⁵ Figure 2 shows Kr II and Xe II equilibrium spectra at 300 K obtained in a low-pressure radiofrequency (RF) discharge. The vacuum wavelength of the Kr II $4d^4F_{7/2} - 5p^2D_{5/2}^0$ transition was accurately measured by means of LIF spectroscopy using two counterpropagating beams to cancel out any drift effect, and we found $\lambda = 820.4959$ nm (820.270 nm in air). This value is lower than the one given in the literature.^{19,20} The Xe II $5d^4F_{7/2} - 6p^2D_{5/2}^0$ transition at 834.9527 nm was previously studied by means of Doppler-free saturation spectroscopy.¹⁸ The wavelength values presented in Figure 2 were

TABLE I. Details of the optical transitions in Kr II and Xe II.^{19–21} λ is the wavelength in a vacuum for the excitation (see Fig. 2) and in air for the fluorescence, E_j and E_k are the initial and final energy bounds, and B_{kj} is the branching ratio.

Single ionized ion	Transition $j \rightarrow k$	λ (nm)	E_j (eV)	E_k (eV)	B_{kj} (%)
Kr II	$4d^4F_{7/2} \rightarrow 5p^2D_{5/2}^0$	820.4959 (vacuum)	15.861	17.372	...
	$5p^2D_{5/2}^0 \rightarrow 5s^2P_{3/2}$	461.917 (air)	17.372	14.689	100
Xe II	$5d^4F_{7/2} \rightarrow 6p^2D_{5/2}^0$	834.9527 (vacuum)	12.589	14.074	...
	$6p^2D_{5/2}^0 \rightarrow 6s^2P_{3/2}$	541.915 (air)	14.074	11.786	100

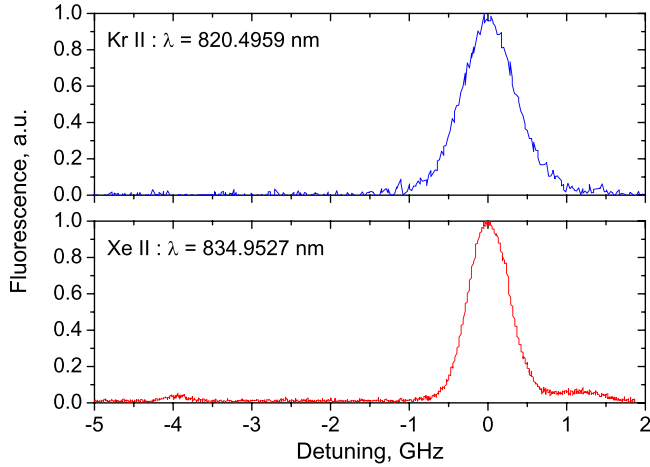


FIG. 2. Normalized fluorescence spectra in arbitrary units as a function of laser detuning in GHz for the $4d^4F_{7/2}$ Kr II and $5d^4F_{5/2}$ Xe II metastable states. λ is the wavelength measured in a vacuum for ions at thermal equilibrium (300 K) in a low-pressure RF discharge; it corresponds to a 0 GHz detuning.

used in this work to determine Doppler shifts. The lower signal-to-noise ratio observed in krypton is related to the high energy of the $4d^4F_{7/2}$ metastable state for Kr II (15.861 eV). The full width at half maximum (FWHM) is $\Delta\nu \approx 0.79$ GHz for Kr II and $\Delta\nu \approx 0.61$ GHz for Xe II. It corresponds to a dispersion in velocities of $\Delta v \approx 648$ m/s for Kr II and $\Delta v \approx 509$ m/s for Xe II. The linewidth depends on the isotopic properties of the atom. Xenon has 7 abundant isotopes, two of which (odd isotopes) have a non-zero nuclear spin. The overall isotope and hyperfine structure for the 834.730 nm line comprises 17 transitions.¹⁸ Krypton has 5 abundant isotopes, one of which has a non-zero nuclear spin. The overall isotope and hyperfine structure for the 820.273 nm line comprises 22 transitions. The LIF profiles measured in xenon and krypton in the plasma of the Hall thruster are much broader than the lineshape for ions at rest at 300 K. Therefore, in the remainder of this work, the LIF profiles are assumed to correspond to the ion VDF.

D. Ion velocity range

For a better understanding, we present in Table II the main terms for the ion velocities that exist in the plasma source. The range covers three orders of magnitude. The ion dynamics in such a cross-field ion source is mainly governed by the electrostatic force that accelerates the ions up to 15 km/s. The ion acoustic velocity originates in the dispersion relation for *ion acoustic waves*²² and provides a lower ion velocity of around 1 km/s. The thermal velocity in Table II depends on the thermal equilibrium of the ions assuming a Maxwellian distribution.

TABLE II. Main ion velocities for Kr II or Xe II in a cross-field ion source.

Ion velocity	Order of magnitude
Electrostatic velocity	$v_E(\mathbf{r}) = \sqrt{2e\Phi(\mathbf{r})/m_i} \approx 10$ km/s
Ion acoustic velocity	$v_{\text{Bohm}}(\mathbf{r}) = \sqrt{kT_e(\mathbf{r})/m_i} \approx 1$ km/s
Thermal velocity	$v_{\text{th}}(\mathbf{r}) = \sqrt{kT_i(\mathbf{r})/m_i} \approx 100$ m/s

TABLE III. Main collisional reactions in xenon and krypton.^{23–25} Cross sections are given for a 100 eV incident ion energy, a 20 eV incident electron energy, and a target atom at rest.

Collisional process	Reaction equation	Cross section (cm ²)
Ionization	$\text{Xe} + e \rightarrow \text{Xe}^+ + 2e$	2.3×10^{-16}
Charge-exchange	$\text{Xe}_{\text{fast}}^+ + \text{Xe}_{\text{slow}} \rightarrow \text{Xe}_{\text{fast}} + \text{Xe}_{\text{slow}}^+$	6×10^{-15}
Ionization	$\text{Kr} + e \rightarrow \text{Kr}^+ + 2e$	1.3×10^{-16}
Charge-exchange	$\text{Kr}_{\text{fast}}^+ + \text{Kr}_{\text{slow}} \rightarrow \text{Kr}_{\text{fast}} + \text{Kr}_{\text{slow}}^+$	4×10^{-15}

In Table III, we identify two collisional reactions in xenon and krypton which influence the ion dynamics. Although the ionization reaction is essential to the ion production, the ion-to-electron mass ratio is too large to bring a significant momentum transfer. Ions are thus created at rest. However, if we assume the charge-exchange reactions to be relevant, one can expect production of ions at low velocities by collisions with neutrals. According to Table II, the cross section for charge-exchange reaction measured both in krypton and xenon is one order of magnitude higher than for ionization.

III. ION AXIAL VDFS ALONG THE SOURCE AXIS

A. In krypton

Figure 3 (top) shows several IVDF profiles in krypton for a few positions along the ion source axis (C-axis). Figure 3 (bottom) is a normalized contourplot of the Kr II axial VDFs represented in the 1D-phase space (x, v_x) at several positions along the ion source axis. It is worth noticing we observe a significant acceleration pattern, whereas no ions are expelled in normal incidence from the center of the ion source since the channel is annular (see Fig. 1). Furthermore, there are two ion groups: one with positive velocities and one with negative velocities. The positive ion velocity group accelerates from 2000 m/s at 3 mm up to 16 000 m/s at 50 mm. The negative velocities ion group appears with thermal speed (≈ 500 m/s) at a location 15 mm downstream the channel exit plane and is accelerated by a negative potential drop toward the source. We ensured this signal was not a beam reflection effect, by repeating this measurement placing a small tilted mirror in the exit plane, facing the laser beam, to avoid a counterpropagating ($-\mathbf{k}$ vector) laser beam. These ions may originate from charge-exchange collisions between the diverging ions and the residual atoms or by local ionization of the residual gas since the electron density remains high and the cathode provides a non-negligible atom flux. The slow ions thus created are subjected to the potential drop between the plasma plume and the ion source, hence they move towards the thruster. The most probable Kr II velocity, i.e., the corresponding velocity for the highest LIF signal, reaches -4000 m/s at 3 mm beyond the exit plane, which corresponds to an accelerating potential of about 6 V (see Fig. 6). In spite of their low kinetic energy, the backflow of these ions generates a significant sputtering of the mounting cross made of aluminium (see Fig. 1). Divergence emphasis is also observed in Figure 3 since no ions observed along the source axis can propagate axially (see Fig. 1). The acceleration shape for the positive ion velocities is thus a geometric effect and is not related to the

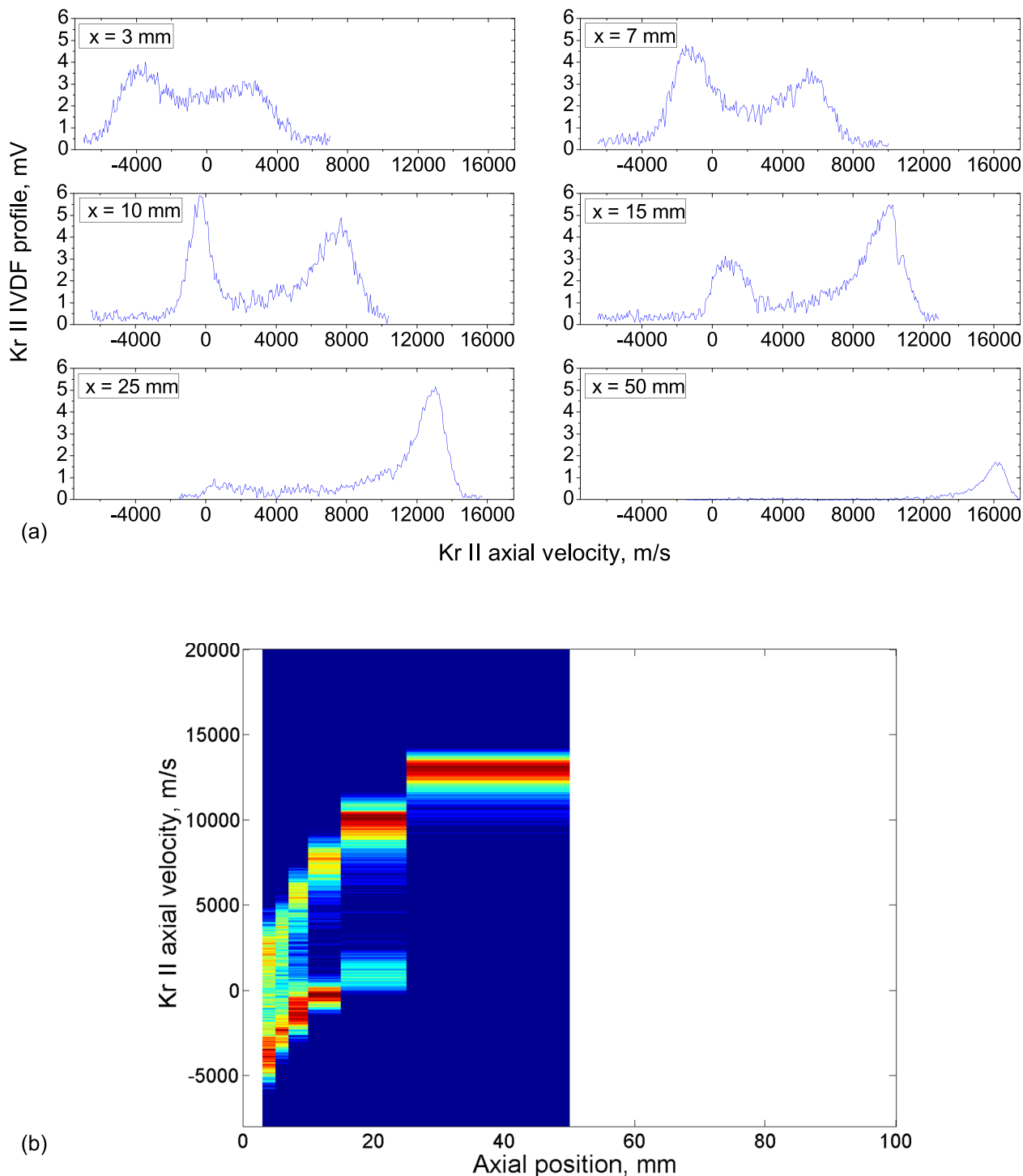


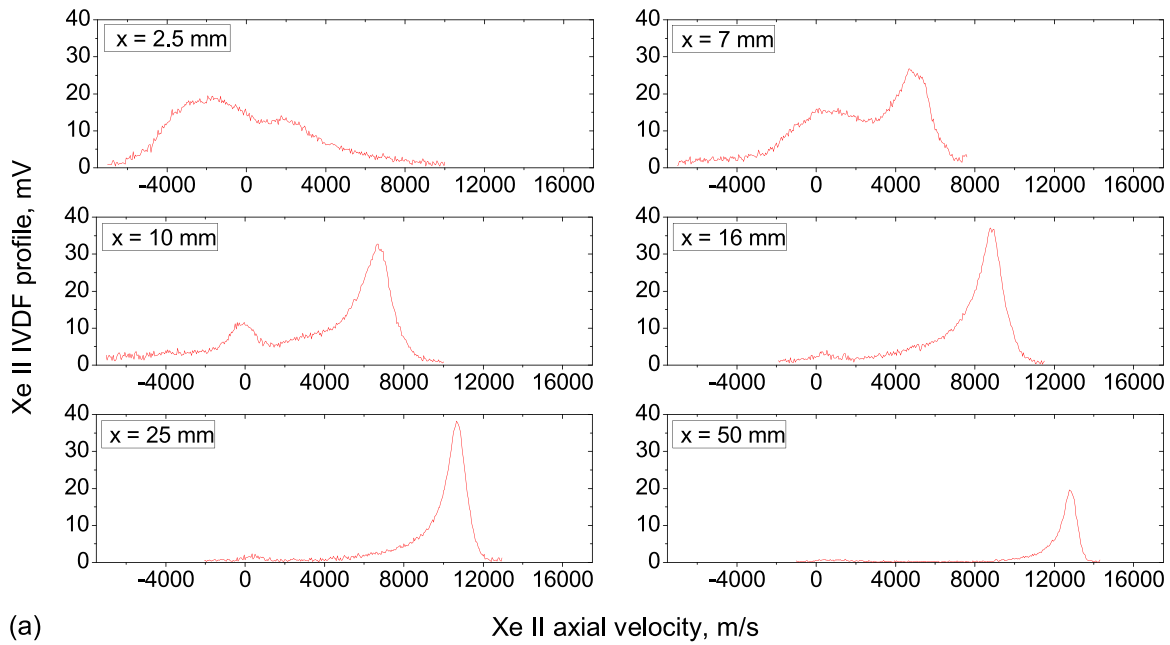
FIG. 3. Top: Kr II axial VDFs profiles as functions of the axial velocity at several locations along the ion source axis (C-axis). Bottom: Normalized contourplot in a 1D-phase space (x, v_x) representation for Kr II axial VDFs.

electric field shape on the source axis. It was shown in previous works^{8,11} that the electric field in such an ion source in Kr cannot be so extended up to 40 mm.

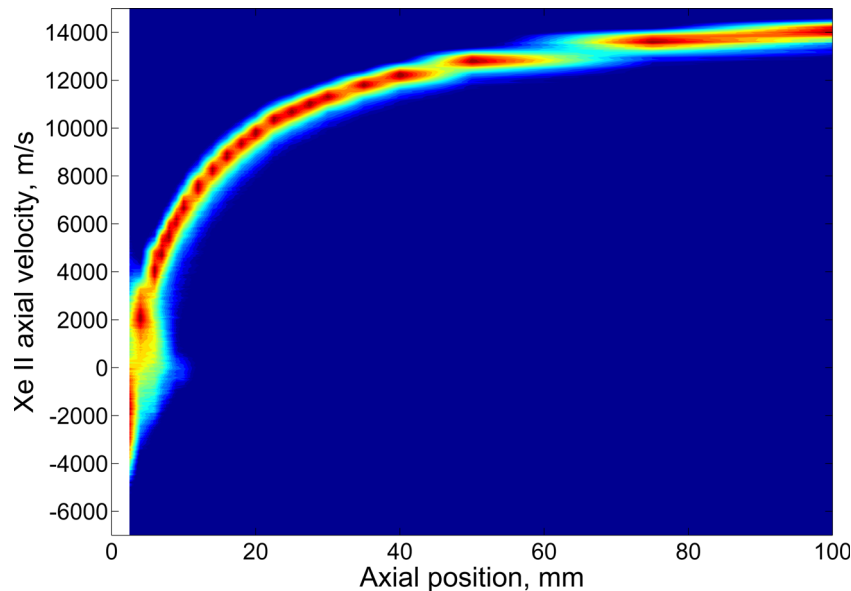
B. In xenon

Figure 4 represents the measurements of the Xe II IVDFs along the centerline. They are similar to the ones carried out in krypton and previously described. In Figure 4 (top), the signal-to-noise ratio (SNR) is clearly higher in xenon than in krypton.

The LIF signal is thus ten times higher in xenon than in krypton since the units of the IVDFs are given in mV for the lock-in with the same sensitivity. A better SNR may come from a larger Xe II population in the metastable $5d\ ^4F_{5/2}$ state than Kr II population in the metastable $4d\ ^4F_{7/2}$ state (Table I). Figure 4 (bottom) represents a normalized contourplot of the Xe II ion axial VDFs in the 1D-phase space (x, v_x) at several positions along the ion source axis up to 100 mm. The ion velocity varies from -4000 m/s at 2.5 mm beyond the exit plane, up to $14\ 000$ m/s at 100 mm. For axial positions from 0 mm to



(a)



(b)

FIG. 4. Top: Xe II axial VDFs profiles as functions of the axial velocity at several locations along the ion source axis (C-axis). Bottom: Normalized contour-plot in a 1D-phase space (x, v_x) representation for Xe II axial VDFs.

15 mm, the ion velocity varies continuously from -4000 m/s to 0 m/s. It corresponds to the slow ion group that is created by charge-exchange collisions and local ionization, previously described in krypton. Likewise, the positive velocity group is related to the axial projection of the velocity vector of ions leaving the annular chamber. Assuming all the ions are mono-kinetics and diverge from a point source localized on the mean diameter, this behaviour agrees with a geometric law in $\cos(\tan^{-1}(1/x))$, where x is the axial position. It is the reason why the curvature observed is so extended beyond the exit plane due to a geometric effect.

C. Beam properties in krypton and xenon

The most probable positive ion velocity density, i.e., the LIF signal corresponding to the positive ion velocity peak, is

observed in Figures 3 and 4 and reported for krypton and xenon in a normalized plot in Figure 5. Assuming the beam is diverging, the profile should reach a maximum when the diverging beam interacts on C-axis (see Fig. 1) giving information about the divergence angle. The two maxima of the profiles in krypton and xenon presented in Figure 5 indicate the plasma plume is slightly more divergent in krypton than in xenon for the same operating point. Another property of the beam is observed through the negative velocity ion groups detected in krypton and xenon in the vicinity of the source central part. Converting the most probable negative velocity v to electrostatic potential ϕ through the relationship $\phi = mv^2/2e$, where m is the ion mass and e is the elementary charge, we plotted in Figure 6 the potential difference profile as a function of the axial position both in krypton and xenon. Although the measurements were not realized up to 0 mm

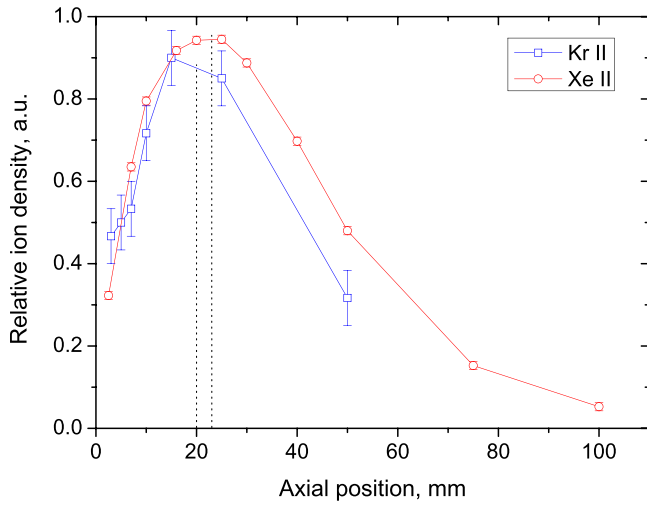


FIG. 5. Normalized profiles of the relative ion density corresponding to the positive ion velocity peak as a function of the axial position along the ion source axis for Kr II and Xe II.

for technical reasons, one observes a potential difference with respect to the plasma potential which is at least two times higher in krypton (6 V) than in xenon (3 V) at 2.5 mm from the exit plane. This behaviour might be a consequence of either a lower floating potential of the thruster or a higher plasma potential in krypton than in xenon. The floating potential of the thruster is related to the electron flux that is trapped in the central magnetic cusp and which depends on the electron temperature which is higher in the exit plane than within the plume.⁸ Such an increase in plasma potential in the vicinity of the exit plane has been also measured⁹ in xenon by emissive probe in the Busek BHT-200 W class device.

IV. ION AXIAL VDFS ALONG THE CHANNEL MEDIAN

A. In krypton

Figure 7 represents the contourplot in a 1D-phase space of the Kr II ion axial VDFs in front of the upper channel (M-axis). The magnitude corresponds to the normalized

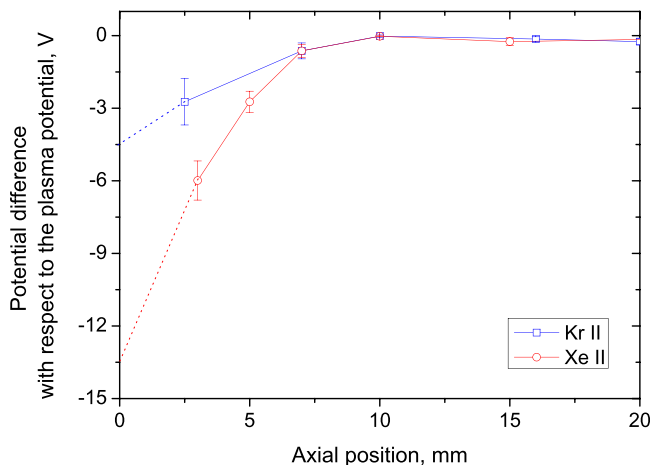


FIG. 6. Potential difference with respect to the plasma potential at 20 mm in the vicinity of the exit plane (0 mm) along the ion source axis for Kr II and Xe II.

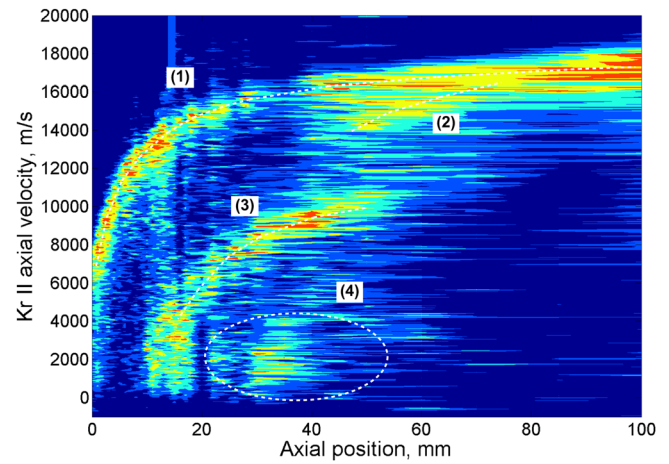


FIG. 7. Normalized contourplot in a 1D-phase space (x, v_x) representation for Kr II axial VDFs in front of the upper channel (M-axis).

signal expressed in arbitrary units and the color scale is adjusted for a good contrast. Although the SNR is low, we clearly identify four different ion groups. The main branch (1) accelerates from 5000 m/s in the channel exit plane up to 16000 m/s at 100 mm. Contrary to the previous measurements along the source axis, this ion group corresponds to the non-diverging incident ions that are axially accelerated from the channel. As was shown in previous works,^{11,13,14,16} the curvature in this case is related to the axial electric field profile. The second branch (2) is located where the electric field is too low to accelerate the ions. As previously shown, the increase in velocities of this group results from the contribution of the axial components of the diverging beam. The apparent acceleration is a mere geometric effect. The third branch (3) appears with velocity from 0 m/s at 10 mm up to 10000 m/s at 50 mm. The slow ions originate either from charge exchange collisions with the main beam (1) or the diverging beam (2) and background residual gas or cathode gas, or from local ionization. The electric field is enough extended up to 10 mm for the slow ions (3) being accelerated. Beyond 50 mm, the third branch (3) is lost in the background noise. The last group (4) is observed with velocities varying between 0 m/s and 4000 m/s. It originates in the slow ions that are created by charge-exchange collisions but at locations too far away from the channel exit plane to be subjected to the maximum of the electric field. They may result from local ionization or interaction with either the main beam (1) or the diverging beam. There is no significant acceleration branch and the ions propagate axially at a constant velocity (≈ 1000 m/s). It is worth noticing this velocity remains in the range of the ion acoustic velocity (see Table II).

B. In xenon

Figure 8 represents the contourplot in a 1D-phase space (x, v_x) of the Xe II ion axial VDFs in front of the upper channel (M-axis). IVDFs are scanned for velocities from 0 m/s to 16000 m/s at several axial positions from 0 mm in the channel exit plane up to 100 mm. The normalized signal is represented as previously in krypton in arbitrary units and the

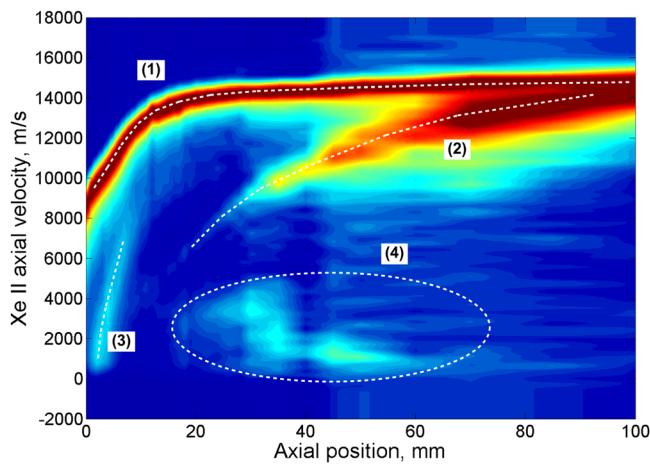


FIG. 8. Normalized contourplot in a 1D-phase space (x, v_x) representation for Xe II axial VDFs in front of the upper channel (M-axis).

color scale is adjusted for good contrast. We observe the main accelerating pattern (1) of the ions that are expelled from the channel. The axial electric field is thus extended up to the location of the null slope of this branch at 25 mm. The velocities grow from 8500 m/s in the channel exit plane up to 14 900 m/s at 100 mm. The initial Xe II velocity in the channel exit plane (1) is higher than that observed in Figure 7 for Kr II, whereas the xenon mass is higher. The electric field in xenon is thus located further back inside the channel than in the krypton case where acceleration is mainly located outside the channel. The second accelerating branch (2) that is observed from 20 mm is a consequence of the geometric effect described previously in krypton and related to the beam divergence. The third branch (3) is observed at positions from 0 mm up to 10 mm with velocities varying continuously from 0 m/s to 8350 m/s. This ion velocity group corresponds to the slow ions that are created by local ionization or charge-exchange with the incident beam (1). Since they are created in the vicinity of the channel exit plane where the electric field is peaked, they are efficiently accelerated like the main branch (1). As in the krypton case, the “ion cloud” (4) appears between 20 mm and 60 mm with low velocities varying from 0 m/s up to 4000 m/s. The decrease in velocity that is observed up to 60 mm confirms that the slow ions created along the axis beyond the maximum of the electric field are less and less accelerated. Far from the channel exit plane at 40 mm, the slow ion velocity thus remains constant in the range value of 1000 m/s that might correspond like in xenon to the ion acoustic velocity (Table II). Such secondary structures were observed in Xe II IVDFs measured in the plasma plume of a low power SPT-50 Hall effect thruster, and the broadened slow ion group at a constant velocity is now identified in the Kr II IVDFs contourplot as a “cloud of slow ions” created by charge-exchange collisions and described by Sadeghi.¹⁶

V. CONCLUSION

Spatially resolved measurements of the axial VDFs for Kr II and Xe II in the plasma plume of a cross-field ion source are achieved using the LIF spectroscopy diagnostic.

Ion axial VDFs observed in space are similar in krypton and xenon. Beyond the standard accelerating pattern that originates in the electrostatic force and generates the thrust, the exploration of secondary structures reveals collisional interactions within the plume which may influence the ion trajectories and thus the spatial extension of the ion beam. In contrast to previous ideas,²⁶ the presence of high energy ions flowing in the near-field plume is explained here considering the annular geometry of the thruster. We show the assumption of a collisionless shock or a double layer due to supersonic beam interaction is not necessary. The beam divergence, the charge-exchange processes, and the presence of a negative potential area are thus observed both in xenon and krypton. A high sputtering on the thruster front face was observed which may be related to the negative potential difference measured between the plasma plume and the thruster body. It is obvious that the charge-exchange processes we observed in laboratory experiments are reduced in real space conditions where the residual pressure is much lower.

ACKNOWLEDGMENTS

This study was performed in the framework of the CNRS/CNES/SNECMA/Universities joint-research program 3161 entitled “Propulsion par plasma dans l’espace.” A. Lejeune benefits from a CNES post-doctoral grant and G. Bourgeois benefits from a SNECMA Ph.D. grant.

- ¹I. G. Brown, *The Physics and Technology of Ion Sources* (Wiley-VCH, Weinheim, 2004).
- ²J. Fuchs *et al.*, “Laser-driven proton scaling laws and new paths toward energy increase,” *Nat. Phys.* **2**, 48–54 (2006).
- ³R. S. Hensworth and T. Inoue, “Positive and negative ion sources for magnetic fusion,” *IEEE Trans. Plasma Sci.* **33**, 1799 (2005).
- ⁴D. M. Goebel and I. Katz, *Fundamentals of Electric Propulsion: Ion and Hall Thrusters*, JPL Space Science and Technology Series (California Institute of Technology, 2008).
- ⁵C. R. Koppel and D. Estublier, “The SMART-1 Hall effect thruster around the moon: In flight experience,” IEPC-2005-119, 2005.
- ⁶V. V. Zhurin, H. R. Kaufman, and R. S. Robinson, “Physics of closed drift thrusters,” *Plasma Sources Sci. Technol.* **8**, R1–R20 (1999).
- ⁷K. Dannenmayer and S. Mazouffre, “Elementary scaling relations for Hall effect thrusters,” *J. Propul. Power* **27**, 236 (2011).
- ⁸J. A. Linnell, “An evaluation of krypton propellant in Hall thrusters,” Ph.D. thesis (University of Michigan, 2007).
- ⁹B. E. Beal, A. D. Gallimore, and W. A. Hargus, “Plasma properties downstream of a low-power Hall thruster,” *Phys. Plasmas* **12**, 123503 (2005).
- ¹⁰A. Lejeune, K. Dannenmayer, G. Bourgeois, and S. Mazouffre, “Impact of the channel width on Hall thruster discharge properties and performances,” IEPC-2011-019, 2011.
- ¹¹G. Bourgeois, A. Lejeune, and S. Mazouffre, “Ion velocity evolution with channel width, magnetic topology and propellant in a 200 W Hall thruster,” IEPC-2011-123, 2011.
- ¹²M. Guyot, P. Renaudin, V. Cagan, and C. Boniface, patent FR 07 05658 (2007).
- ¹³D. Gawron, S. Mazouffre, N. Sadeghi, and A. Héron, “Influence of magnetic field and discharge voltage on the acceleration layer features in a Hall effect thruster,” *Plasma Sources Sci. Technol.* **17**, 025001 (2008).
- ¹⁴S. Mazouffre, V. Kulaev, and J. Pérez Luna, “Ion diagnostics of a discharge in crossed electric and magnetic fields for electric propulsion,” *Plasma Sources Sci. Technol.* **18**, 034022 (2009).
- ¹⁵W. Hargus, G. M. Azarnia, and M. R. Nakles, “Demonstration of Laser-Induced Fluorescence on a krypton Hall effect thruster,” IEPC-2011-018, 2011.
- ¹⁶N. Sadeghi, N. Dorval, C. Philippe *et al.*, “Velocity measurements of Xe⁺ in stationary plasma thruster using LIF,” AIAA-99-2429, 1999.

- ¹⁷W. Demtröder, *Laser Spectroscopy, Basic Concepts and Instrumentation*, 2nd ed. (Springer-Verlag, Berlin, 1998).
- ¹⁸E. Pawelec, S. Mazouffre, and N. Sadeghi, "Hyperfine structure of some near-infrared Xe I and Xe II lines," *Spectrochim. Acta, Part B* **66**, 470 (2011).
- ¹⁹See <http://www.nist.gov/pml/data/asd.cfm> for NIST atomic spectra database.
- ²⁰K. Dzierżęga, U. Griesmann, G. Nave, and L. Bratasz, "Absolute transition rates for transitions from 5 p levels in Kr II," *Phys. Scr.* **63**, 209 (2001).
- ²¹S. Zielińska, L. Bratasz, and K. Dzierżęga, "Absolute transition rates for transitions from $5p^4(^3P)6p^4P_{5/2}^0$, $4P_{3/2}^0$, $4D_{7/2}^0$ and $2D_{5/2}^0$ levels of Xe II," *Phys. Scr.* **66**, 454 (2002).
- ²²F. F. Chen, *Plasma Physics and Controlled Fusion, Volume 1: Plasma Physics*, 2nd ed. (Springer, 1983).
- ²³See <http://www-admis.iaea.org/ALADDIN/collisions.html> for IAEA AMDIS ALADDIN database.
- ²⁴J. S. Miller, S. H. Pullins, D. J. Levandier *et al.*, "Xenon charge exchange cross sections for electrostatic thruster models," *J. Appl. Phys.* **91**, 984 (2002).
- ²⁵B. M. Smirnov, "Atomic structure and the resonant charge exchange process," *Phys. Usp.* **44**, 221 (2001).
- ²⁶V. Hruby, J. Monheiser, B. Pote *et al.*, "Development of low power Hall thrusters," AIAA-99-3534, 1999.